Aorta Multi-class Segmentation via Anatomically Constrained Plane Detection

Jonghoon An[1], Dong Hyun Lee[1], So Hyun Kim[1], Taejin Moon[1], and Minyoung Chung[1]*

School of Software, Soongsil University, Seoul, Republic of Korea
`chungmy@ssu.ac.kr`

Abstract. Accurate multi-class segmentation of the aorta in medical CT images is essential for the effective diagnosis and treatment of blood flow abnormalities. However, achieving precise segmentation in multi-zone remains challenging due to the lack of visible boundaries and the similarity in intensity between zones. Although existing methods incorporate anatomical features such as global geometric constraints and landmark-based alignment, they often struggle when these features are difficult to extract, such as in regions with asymmetric deformation or extreme curvature due to dissection. This limitation of relying solely on simple anatomical cues underscores the need to learn and model complex anatomical interrelationships for robust segmentation. To overcome these challenges, we propose a plane detection-based segmentation framework that is constrained by anatomical features and their relationships to accurately detect planes between zones. Specifically, our method detects planes by localizing centerpoints and regressing the corresponding normal vectors, while anatomical landmarks further refine the position and orientation of these planes. Additionally, anatomical regularization losses enforce geometric consistency among these components, thereby enhancing both accuracy and stability of the detected planes. The entire framework is implemented as an end-to-end architecture, enabling efficient learning. The experimental results on the AortaSeg24 dataset demonstrate that our approach achieves state-of-the-art performance. Our code is publicly available at https://github.com/jjong0225/ACP.

Keywords: Anatomical constraints · Anatomical regularization · Aorta multi-class segmentation · Plane detection.

1 Introduction

Aortic segmentation in medical CT images is a critical step in various clinical procedures, particularly for addressing blood flow abnormalities [1–3]. For successful interventions, detailed structural and functional analysis is essential, which is achieved by dividing the aorta into multiple zones based on clinically relevant anatomical definitions, such as the Society for Vascular Surgery/Society

---

[*] Corresponding author

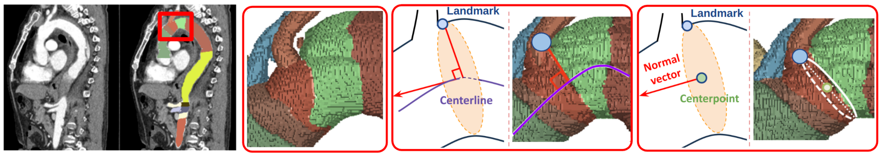

(a) (b) (c) (d)

Fig. 1. (a) Multi-zone image and label. (b) Previous works (SwinUNETR [6]). (c) Anatomical definition of multi-zone class boundaries with ground-truth. (d) Proposed plane detection-based segmentation (Ours).

of Thoracic Surgeons (SVS/STS) zones. [4]. Multi-zone segmentation enables the automated measurements of the diameters and volumes, which are essential for accurate device selection, and precise stent placement [5]. Given that these measurements directly impact treatment efficacy [7], achieving high segmentation accuracy is paramount [5, 8]. While considerable progress has been made in aortic segmentation, multi-zone segmentation remains challenging due to the inherent similarity of class intensities and the lack of clear boundaries between zones (Fig. 1a, b).

To address these challenges, significant research has leveraged anatomical knowledge to constrain segmentation outputs in line with expected anatomical properties [9–15]. Since inter-zone planes are defined by the aortic structure and its landmarks (Fig. 1c), two primary strategies have emerged: imposing geometric constraints across zones [5, 9–11] and aligning planes using landmarks [12–14]. Geometric constraints approaches focus on constraining structural consistency across zones. In the AortaSeg24 challenge [5], A5 employed Skeleton Recall Loss [16] to ensure connectivity, while A2 applied centerline boundary Dice [17] to enhance centerline integrity. Conversely, landmark-driven plane approaches directly define planes by leveraging landmarks and centerlines. The planes are defined to pass through the detected landmarks while being orthogonal to the centerline (Fig. 1c). For example, [12] derived landmarks through curvature analysis, whereas [13] incorporated an auxiliary network for landmark prediction. Although these studies resolve visually ambiguous multi-zone boundaries, they often struggle to produce accurate segmentation when these features are poorly extracted such as in regions with asymmetric deformation or extreme curvature due to dissection [15, 18]. This limitation of relying solely on simple anatomical cues underscores the need to learn and model complex anatomical interrelationships for robust segmentation.

In this paper, we propose an anatomically constrained plane detection–based segmentation framework that ensures accurate, anatomically aligned planes. Specifically, the framework decomposes the plane into three components: (1) the centerpoint, which defines its approximate location along the centerline, (2) landmarks, which serve as anatomical reference points to guide both its location and alignment, and (3) the normal vector, which determines its precise alignment by accounting for the aortic structure. Furthermore, our anatomical regularization enforces the geometric relationships among these components. This guarantees that the predicted planes adhere to the anatomical priors, thus improving segmentation accuracy. We implemented the entire framework including segmentation and plane detection into an end-to-end framework, enabling efficient learning.

To summarize, the contributions of this study are as follows:

- We propose a novel plane detection–based segmentation framework.
- We introduce an anatomy-constrained plane detection that learns the anatomical components of planes and their geometric relationships.
- We implemented an efficient end-to-end architecture that jointly learns plane detection and aortic segmentation.
- Our framework outperforms state-of-the-art methods in segmentation accuracy on the AortaSeg24 dataset.

2 Anatomically Constrained Plane Detection

We propose an anatomically constrained plane detection-based segmentation framework. An overview of our framework is illustrated in Fig. 2a. Our framework employs plane detection to address visually ambiguous boundaries by integrating anatomical constraints. Specifically, we model each plane with three key components (centerpoints, landmarks, and normal vectors) and learn their anatomical relationships. The plane position is first estimated using centerpoints and landmarks extracted from a keypoint detection head (Fig. 2b, Section 2.1). Then, the normal vector for each plane class, conditioned on the centerpoints and landmarks of the corresponding class, is estimated via a normal vector regression head (Fig. 2b, Section 2.2). Finally, an anatomical regularization term is applied to capture the geometric relationship among these components (Fig. 2c, Section 2.3).

2.1 Centerpoint and Landmark Detection

Our framework detects planes using seven arterial branch landmarks and nine centerpoints derived from their centerline (Fig. 2a). Specifically, landmarks are identified as the arterial branches closest to the boundary points, while the centerpoints represent the midpoints of the boundaries between adjacent zones.

To obtain keypoints $\mathbf{K}$, composed of landmarks $\mathbf{L}$ and centerpoints $\mathbf{C}$, we adopt a heatmap-based keypoint detection framework following [13]. This approach estimates keypoints by learning their spatial probability distribution. Specifically, shared features $\mathbf{f}_{share}$ are passed through a keypoint detection head (KD Head), composed of convolutional layers, to generate heatmaps for landmarks $\mathbf{h_L}$ and centerpoints $\mathbf{h_C}$ (Fig. 2b). These heatmaps are converted into trainable keypoint coordinates using keypoint localization, which computes the weighted mean of the heatmap and the coordinate map $\mathbf{r}$ through element-wise multiplication, as follows:

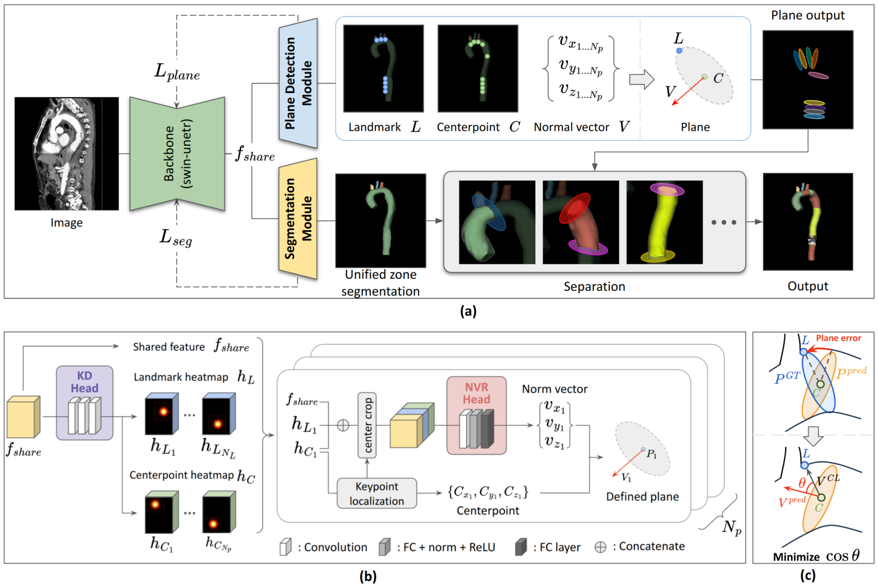

Fig. 2. (a) Overview of our framework for plane-based multi-class segmentation, where multi-zone segmentation is defined by partitioning the predicted unified zone segmentation with detected planes. (b) Plane detection module estimates class-wise planes using centerpoint and normal vector. The keypoint detection head (KD Head) generates heatmaps for landmarks and centerpoints, which are then fused with features and passed to the normal vector regression head (NVR Head) to predict class-specific normal vectors. (c) Anatomical regularization refines planes by enforcing geometric constraints among anatomical components. Plane error, visualized as the blue-orange discrepancy, is quantified by the angle θ between V^{pred} and V^{CL}. Enforcing $\theta = 90°$ minimizes the error and ensures anatomical consistency.

$$\mathbf{K} = \frac{\sum_{x,y,z} h(x,y,z) \cdot \mathbf{r}(x,y,z)}{\sum_{x,y,z} h(x,y,z)}, \tag{1}$$

where $\mathbf{r}(x,y,z)$ is the spatial coordinates and $h(x,y,z)$ is the heatmap value. To train the model with heatmaps, we use Gaussian heatmaps centered on keypoints as ground truth (GT) and optimize the model using focal loss $\mathcal{L}_{\text{key}}$ [14], following [13].

2.2 Normal Vector Regression

We directly predict the parametric representation of a plane by regressing its normal vector $\mathbf{V} = (v_x, v_y, v_z)$. To ensure that the predicted normal vector aligns with the centerpoints and anatomical landmarks (Fig. 2b), class-specific normal vectors are regressed while being conditioned on the corresponding keypoint heatmap predictions. Specifically, the regression pipeline begins with the shared features $\mathbf{f}_{share}$ and keypoint heatmaps ($\mathbf{h}_L$ and $\mathbf{h}_C$) as inputs. These inputs are cropped around the detected centerpoints, focusing on the regions of interest. The cropped features are then fed into the normal vector regression head (NVR Head), which predicts the normal vector $\mathbf{V}^{pred}$ through a series of convolution layers and fully connected layers (Fig 2b). For training, we minimize the vector regression loss $\mathbf{L}_{vec}$, which penalizes the L1 difference between predicted normal vectors $\mathbf{V}^{pred}$ and GT normal vectors $\mathbf{V}^{GT}$, as follows:

$$\mathcal{L}_{vec} = \frac{1}{N_p} \sum_{i=1}^{N_p} \left\| \mathbf{V}_i^{pred} - \mathbf{V}_i^{gt} \right\|_1 . \tag{2}$$

2.3 Anatomical Regularization

To ensure geometric consistency across predicted plane components, we introduce an anatomical regularization. This regularization leverages the anatomical definition of multi-zone regions, where the centerpoint and landmark vector of each plane are constrained to lie on that plane defined by the normal vector (Fig. 2c).

Specifically, we first convert the heatmap into landmark and centerpoint coordinates using (1). We then compute the centerpoint–landmark vector $\mathbf{V}^{CL}$ by subtracting the centerpoint from the landmark and normalizing it. Finally, we measure the orthogonality between the $\mathbf{V}^{CL}$ and the $\mathbf{V}^{pred}$ using cosine similarity, which is incorporated into the anatomical regularization loss $\mathcal{L}_{reg}$, as follows:

$$\mathcal{L}_{reg} = \frac{1}{N_p} \sum_{i=1}^{N_p} \left(\mathbf{V}_i^{CL} \cdot \mathbf{V}_i^{pred} \right)^2 . \tag{3}$$

Minimizing $\mathcal{L}_{reg}$ enforces geometrical consistency among the plane's components, preserving anatomical structure and enabling accurate segmentation.

2.4 End-to-End Architecture

We implemented an end-to-end architecture that jointly trains plane detection and aortic segmentation. The process begins with a shared backbone that extracts shared features, $\mathbf{f}_{share}$, which are then fed to task-specific modules for plane detection and segmentation. By jointly learning from a shared representation, each module remains independent in its predictions while leveraging shared information, enhancing efficiency and consistency across tasks. We employ SwinUNETR [6] as the shared backbone and segmentation framework for unified zone class and 13 artery classes. Following its original implementation, the model optimizes a segmentation loss $\mathcal{L}_{seg}$ combining Dice loss [14] and Focal loss [19]. All losses are integrated into a joint loss formulation, as follows:

$$\mathcal{L}_{total} = \mathcal{L}_{seg} + \lambda_{key}\mathcal{L}_{key} + \lambda_{vec}\mathcal{L}_{vec} + \lambda_{reg}\mathcal{L}_{reg}, \tag{4}$$

where λ_{key}, λ_{vec}, and λ_{reg} are weighting coefficients for $\mathcal{L}_{key}$, $\mathcal{L}_{vec}$, and $\mathcal{L}_{reg}$, respectively.

3 Experiments

Experiments were conducted on the AortaSeg24 Challenge dataset [5], the only publicly available benchmark for multi-class segmentation of aortic structures in CTA scans. The dataset is divided into 40 training and 10 test cases. All images were resampled to an isotropic resolution of $1\mathrm{mm}^{\mathbf{3}}$, intensity-normalized to [0,1], and cropped using labels. Additional labels for plane parameters are derived using the centroid and principal component analysis (PCA) of class boundary points. The derived ground truth (GT) plane parameters effectively characterize the segmentation structure, achieving a Dice Similarity Coefficient [20] of 0.9732 for the segmentation obtained through plane-based separation. During the test phase, this separation process involves refining the predicted segmentation by extracting the largest connected component, followed by partitioning into subregions based on the predicted plane parameters. Each subregion is then assigned a class label corresponding to its associated plane.

All models, including our proposed method and competing baselines, were trained from scratch without any pre-training, under identical conditions and rigorously tuned to ensure fair comparison.

3.1 Evaluation Metrics

We evaluate segmentation performance using the Dice Similarity Coefficient (DSC), the 95th percentile hausdorff distance (HD95), and the average symmetric surface distance (ASSD). DSC quantifies the overlap ratio between the predicted and GT segmentations, providing a measure of overall segmentation accuracy. In contrast, HD95 and ASSD assess surface-based errors, capturing the geometric discrepancy between predicted and GT planes.

Additionally, to assess clinical adaptability, we include diameter measurements, which are crucial for applications such as surgical planning, device selection, and minimally invasive interventions [21]. Specifically, we define the diameter error (DE) as the absolute difference in distance between the predicted and GT diameters, measured in millimeters (mm).

3.2 Experimental Results

For evaluation, we compare two widely used segmentation models (3D U-Net [22] and SwinUNETR [6]) along with three aortic segmentation models (CIS-UNet [23], A5 [5], an nnU-Net [24] variant model with geometric constraints, and M-SL [13], a landmark-driven plane approach). Table 1 presents the quantitative segmentation performance, reporting the mean values of DSC, HD95, ASSD, and DE. Our method outperforms the baseline SwinUNETR and multiple state-of-the-art (SOTA) approaches, demonstrating superior segmentation accuracy, surface delineation, and clinical applicability.

Our model improves DSC by 10.5% over the baseline and by 6% over CIS-UNet, the best-performing method for DSC, demonstrating consistently higher segmentation accuracy. Beyond DSC, our method reduces HD95 by 33% and

Table 1. Segmentation performance comparison (mean ± std). Higher is better for DSC (↑); lower is better for HD95, ASSD, and DE (↓).

Method	**DSC ↑**	**HD95 ↓**	**ASSD ↓**	**DE ↓**
3D U-Net [22]	0.729 ± 0.064	8.875 ± 2.98	2.444 ± 0.79	6.328 ± 1.83
SwinUNETR [6]	0.718 ± 0.057	9.044 ± 3.00	2.484 ± 0.76	5.471 ± 2.03
CIS-UNet [23]	0.748 ± 0.063	8.360 ± 2.77	2.249 ± 0.75	4.810 ± 1.86
A5 [5]	0.750 ± 0.045	7.587 ± 2.45	2.156 ± 0.57	3.992 ± 1.18
M-SL [13]	0.732 ± 0.060	8.483 ± 2.18	2.266 ± 0.64	3.453 ± 1.40
Ours	**0.793 ± 0.039**	**5.990 ± 2.06**	**1.745 ± 0.43**	**3.016 ± 1.11**

Table 2. Zone-wise DSC performance for each zone, denoted as Z_i, where i represents the zone index.

Method	Z_0	Z_1	Z_2	Z_3	Z_4	Z_5	Z_6	Z_7	Z_8	Z_9
3D U-Net [22]	0.919	0.619	0.712	0.706	0.715	0.858	0.668	0.599	0.635	0.855
SwinUNETR [6]	0.905	0.597	0.729	0.720	0.749	0.869	0.520	0.587	0.625	0.879
CIS-UNet [23]	**0.926**	0.656	0.719	0.667	0.748	0.882	0.648	0.661	0.689	0.884
A5 [5]	0.895	0.592	0.709	0.693	0.796	0.884	0.690	0.654	0.680	0.903
M-SL [13]	0.908	0.613	0.717	0.705	0.783	0.863	0.577	0.608	0.678	0.866
Ours	0.924	**0.666**	**0.752**	**0.726**	**0.827**	**0.900**	**0.759**	**0.731**	**0.740**	**0.908**

ASSD by 31% compared to the baseline and by 28% and 22%, respectively, compared to A5, the best-performing method for surface accuracy. These results highlight our method's precise plane detection, reducing noise and improving segmentation accuracy. Furthermore, DE is reduced by 40% compare to the baseline and by 24% compared to M-SL, the best-performing method for DE. This improvement underscores our method's adaptability to clinical applications by precisely estimating diameters through accurate and stable plane detection. The consistently lower standard deviations across all metrics further confirm that our improvements are not driven by outlier handling, but reflect robust and consistent performance gains across cases, including those with asymmetric deformation or extreme curvature. Table 2 further validates these findings, demonstrating consistent performance gains across most anatomical zones, except for Zone 0. Fig. 3 qualitatively illustrates that our method produces accurate plane, whereas SOTA methods exhibit increased noise and structural inconsistencies. These results reinforce the effectiveness of our approach in both segmentation accuracy and clinical reliability.

3.3 Ablation Study of Plane Detection

To assess the impact of individual components in our anatomically constrained plane detection framework, we performed an ablation study under consistent experimental settings. The study began with the baseline, followed by progressive additions of key components : (1) landmarks, (2) plane detection, and (3) anatomical regularization.

Table 3 presents the results, demonstrating that each component incrementally improves segmentation accuracy. The introduction of anatomical landmarks

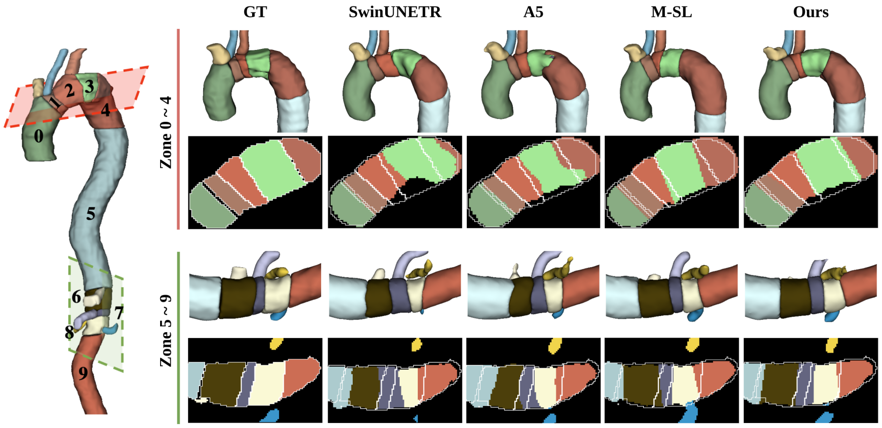

Fig. 3. Qualitative comparison of registration methods. The left panel visualizes overall zone locations and slice positions for comparison. The right panels present qualitative comparison, with the GT class boundary shown as a white contour. While other methods exhibit segmentation noise or inaccuracies in plane delineation, our approach achieves precise segmentation and plane estimation that closely aligns with the GT.

Table 3. Ablation study on our anatomically constrained plane detection framework.

Method	**DSC ↑**	**HD95 ↓**	**ASSD ↓**	**DE ↓**
Baseline (SwinUNETR [6])	0.7179	9.0437	2.4843	5.4712
+ landmark	0.7205	8.4696	2.3384	3.1487
+ plane detection	0.7682	7.2032	2.0194	3.1319
+ anatomical regularization	**0.7932**	**5.9906**	**1.7452**	**3.0159**

improves segmentation accuracy by defining a landmark-driven plane, reducing HD95 by 6.35%, ASSD by 5.87%, and DE by 42.45%. This suggest that leveraging anatomical priors effectively delineates ambiguous boundaries, mitigating noise and inaccuracies. Incorporating plane detection further enhances segmentation by providing spatial priors for both position and orientation, leading to a 6.62% improvement in DSC. This underscores the effectiveness of integrating multiple anatomical priors to refine segmentation accuracy. Finally, anatomical regularization enforces geometric consistency, further reducing HD95 by 16.83%, ASSD by 13.58% and improving DSC by 3.25%. This suggest that beyond a simple combination of anatomical cues, modeling the interrelations among plane components enables more precise and robust segmentation. These results suggest that leveraging anatomical priors guides segmentation toward anatomically consistent and robust outcomes.

4 Conclusion

We presented an anatomically constrained plane detection-based segmentation framework for aortic multi-class segmentation. Our framework models the complex anatomical interrelationships of planes, ensuring not only high segmentation accuracy but also precise estimation of clinically relevant metrics. While our current work focuses on multi-zone segmentation of the aorta, future efforts will extend this methodology to other vascular structures, such as arteries, to further validate its generalizability and clinical utility.

Acknowledgments. This work was supported by the Material&parts technology development project (20024280, Development of a Focused Ultrasound Therapeutic Device for BBB Opening and Neuromodulation) funded By the Ministry of Trade, Industry & Energy(MOTIE, Korea).

Disclosure of Interests. The authors have no competing interests to declare that are relevant to the content of this article.

References

1. Mavridis, C., Economopoulos, T.L., Benetos, G., Matsopoulos, G.K.: Aorta segmentation in 3d ct images by combining image processing and machine learning techniques. Cardiovascular Engineering and Technology **15**(3), 359–373 (2024)
2. Mayer, C., Arnreiter, M., Karner, B., Hossain, S., Deutschmann, H., Zimpfer, D., Mächler, H.: Aortic segmentations and their possible clinical benefits. In: MICCAI Challenge on Segmentation of the Aorta, pp. 135–140. Springer (2023)
3. Lareyre, F., Yeung, K.K., Guzzi, L., Di Lorenzo, G., Chaudhuri, A., Behrendt, C.A., Spanos, K., Raffort, J.: Artificial intelligence in vascular surgical decision making. In: Seminars in Vascular Surgery. vol. 36, pp. 448–453. Elsevier (2023)
4. Lombardi, J.V., Hughes, G.C., Appoo, J.J., Bavaria, J.E., Beck, A.W., Cambria, R.P., Charlton-Ouw, K., Eslami, M.H., Kim, K.M., Leshnower, B.G., et al.: Society for vascular surgery (svs) and society of thoracic surgeons (sts) reporting standards for type b aortic dissections. The Annals of thoracic surgery **109**(3), 959–981 (2020)
5. Imran, M., Krebs, J.R., Sivaraman, V.B., Zhang, T., Kumar, A., Ueland, W.R., Fassler, M.J., Huang, J., Sun, X., Wang, L., et al.: Multi-class segmentation of aortic branches and zones in computed tomography angiography: The aortaseg24 challenge. arXiv preprint arXiv:2502.05330 (2025)
6. Hatamizadeh, A., Nath, V., Tang, Y., Yang, D., Roth, H.R., Xu, D.: Swin unetr: Swin transformers for semantic segmentation of brain tumors in mri images. In: International MICCAI brainlesion workshop. pp. 272–284. Springer (2021)
7. Mendoza, D.D., Kochar, M., Devereux, R.B., Basson, C.T., Min, J.K., Holmes, K., Dietz, H.C., Milewicz, D.M., LeMaire, S.A., Pyeritz, R.E., et al.: Impact of image analysis methodology on diagnostic and surgical classification of patients with thoracic aortic aneurysms. The Annals of thoracic surgery **92**(3), 904–912 (2011)
8. Krebs, J.R., Imran, M., Fazzone, B., Viscardi, C., Berwick, B., Stinson, G., Heithaus, E., Upchurch Jr, G.R., Shao, W., Cooper, M.A.: Volumetric analysis of acute uncomplicated type b aortic dissection using an automated deep learning aortic zone segmentation model. Journal of Vascular Surgery **80**(4), 1025–1034 (2024)
9. Xie, L., Chen, Z., Sheng, X., Zeng, Q., Huang, J., Wen, C., Wen, L., Xie, G., Feng, Y.: Semi-supervised region-connectivity-based cerebrovascular segmentation for time-of-flight magnetic resonance angiography image. Computers in Biology and Medicine **149**, 105972 (2022)

10. Shit, S., Paetzold, J.C., Sekuboyina, A., Ezhov, I., Unger, A., Zhylka, A., Pluim, J.P., Bauer, U., Menze, B.H.: cldice-a novel topology-preserving loss function for tubular structure segmentation. In: Proceedings of the IEEE/CVF conference on computer vision and pattern recognition. pp. 16560–16569 (2021)
11. Chen, D., et al.: Multi-stage learning for segmentation of aortic dissections using a prior aortic anatomy simplification. Medical Image Analysis **69**, 101931 (2021)
12. Pirentis, A., Kalogerakos, P.D., Mojibian, H., Elefteriades, J.A., Lazopoulos, G., Papaharilaou, Y.: Automated ascending aorta delineation from ecg-gated computed tomography images. Medical & Biological Engineering & Computing **60**(7), 2095–2108 (2022)
13. Yang, J., Li, X., Cheng, J.Z., Xue, Z., Shi, F., Ji, Y., Wang, X., Yang, F.: Segment aorta and localize landmarks simultaneously on noncontrast ct using a multitask learning framework for patients without severe vascular disease. Computers in Biology and Medicine **160**, 107002 (2023)
14. Saitta, S., Sturla, F., Caimi, A., Riva, A., Palumbo, M.C., Nano, G., Votta, E., Corte, A.D., Glauber, M., Chiappino, D., et al.: A deep learning-based and fully automated pipeline for thoracic aorta geometric analysis and planning for endovascular repair from computed tomography. Journal of digital imaging **35**(2), 226–239 (2022)
15. Pepe, A., Egger, J., Codari, M., Willemink, M.J., Gsaxner, C., Li, J., Roth, P.M., Schmalstieg, D., Mistelbauer, G., Fleischmann, D.: Automated cross-sectional view selection in ct angiography of aortic dissections with uncertainty awareness and retrospective clinical annotations. Computers in Biology and Medicine **165**, 107365 (2023)
16. Kirchhoff, Y., Rokuss, M.R., Roy, S., Kovacs, B., Ulrich, C., Wald, T., Zenk, M., Vollmuth, P., Kleesiek, J., Isensee, F., et al.: Skeleton recall loss for connectivity conserving and resource efficient segmentation of thin tubular structures. In: European Conference on Computer Vision. pp. 218–234. Springer (2024)
17. Shi, P., Hu, J., Yang, Y., Gao, Z., Liu, W., Ma, T.: Centerline boundary dice loss for vascular segmentation. In: International Conference on Medical Image Computing and Computer-Assisted Intervention. pp. 46–56. Springer (2024)
18. Kaladji, A., Spear, R., Hertault, A., Sobocinski, J., Maurel, B., Haulon, S.: Centerline is not as accurate as outer curvature length to estimate thoracic endograft length. European Journal of Vascular and Endovascular Surgery **46**(1), 82–86 (2013)
19. Lin, T.Y., Goyal, P., Girshick, R., He, K., Dollár, P.: Focal loss for dense object detection. In: Proceedings of the IEEE international conference on computer vision. pp. 2980–2988 (2017)
20. Dice, L.R.: Measures of the amount of ecologic association between species. Ecology **26**(3), 297–302 (1945)
21. Artzner, C., Bongers, M.N., Kärgel, R., Faby, S., Hefferman, G., Herrmann, J., Nopper, S.L., Perl, R.M., Walter, S.S.: Assessing the accuracy of an artificial intelligence-based segmentation algorithm for the thoracic aorta in computed tomography applications. Diagnostics **12**(8), 1790 (2022)
22. Çiçek, Ö., Abdulkadir, A., Lienkamp, S.S., Brox, T., Ronneberger, O.: 3d u-net: learning dense volumetric segmentation from sparse annotation. In: Medical Image Computing and Computer-Assisted Intervention–MICCAI 2016: 19th International Conference, Athens, Greece, October 17-21, 2016, Proceedings, Part II 19. pp. 424–432. Springer (2016)

23. Imran, M., Krebs, J.R., Gopu, V.R.R., Fazzone, B., Sivaraman, V.B., Kumar, A., Viscardi, C., Heithaus, R.E., Shickel, B., Zhou, Y., et al.: Cis-unet: Multi-class segmentation of the aorta in computed tomography angiography via context-aware shifted window self-attention. Computerized Medical Imaging and Graphics **118**, 102470 (2024)
24. Isensee, F., Jaeger, P.F., Kohl, S.A., Petersen, J., Maier-Hein, K.H.: nnu-net: a self-configuring method for deep learning-based biomedical image segmentation. Nature methods **18**(2), 203–211 (2021)